Few-Body Systems

$\gamma n(p)\rightarrow\pi^-p(p)$ Asymmetries with Linearly Polarized Beam and Longitudinally Polarized Targets in N* Resonance Region

--Manuscript Draft--

Manuscript Number:	FBSY-D-18-00126R2
Full Title:	$\gamma n(p)\rightarrow\pi^-p(p)$ Asymmetries with Linearly Polarized Beam and Longitudinally Polarized Targets in N* Resonance Region
Article Type:	T.C. : NSTAR 2017
Corresponding Author:	Haiyun Lu University of Iowa Peachtree Corners, GA UNITED STATES
Corresponding Author Secondary Information:	
Corresponding Author's Institution:	University of Iowa
Corresponding Author's Secondary Institution:	
First Author:	Haiyun Lu
First Author Secondary Information:	
Order of Authors:	Haiyun Lu
Order of Authors Secondary Information:	
Funding Information:	U.S. Department of Energy (DE-AC05-06OR23177) — Not applicable
Abstract:	The excited-state spectrum of the nucleon is a complicated overlap of many resonances that must be disentangled through multipole analyses of reaction amplitudes. Meson photoproduction, which has been a fruitful probe of N* structure, requires data on many different polarization observables to constrain its four complex amplitudes. While considerable data has been accumulated with proton targets, comparatively little information is available from neutron targets. Recently, the first beam-target helicity asymmetries with circular beam polarization in the $\gamma n(p)\rightarrow\pi^-p(p)$ reaction have been reported. This talk presents a parallel analysis from the same experiment of the beam-target double-polarization observable "G" with linearly polarized beam for the same reaction. Linearly polarized photons and longitudinally polarized deuterons in a solid hydrogen deuteride (HD) target were used with the CEBAF Large Acceptance Spectrometer (CLAS) at Jefferson lab (JLab). Data are combined to extract the beam (Σ) and beam-target (G) asymmetries. Preliminary results for the Σ observables are consistent with existing partial wave analysies (PWA) that incorporate other experiments. Preliminary results for the energy and angular dependence of G are reported; these deviate strongly from existing PWA.
Response to Reviewers:	Modified as instructed.

Noname manuscript No.
(will be inserted by the editor)

$\gamma n(p) \to \pi^- p(p)$ Asymmetries with Linearly Polarized Beams and Longitudinally Polarized Targets in the N^* Resonance Region

H. Y. Lu for the g14 Analysis Group and the CLAS Collaboration

Received: date / Accepted: date

Abstract The excited-state spectrum of the nucleon is a complicated overlap of many resonances that must be disentangled through multipole analyses of reaction amplitudes. Meson photoproduction, which has been a fruitful probe of N^* structure, requires data on many different polarization observables to constrain its four complex amplitudes. While considerable data has been accumulated with proton targets, comparatively little information is available from neutron targets. Recently, the first beam-target helicity asymmetries with circular beam polarization in the $\gamma n(p) \to \pi^- p(p)$ reaction have been reported [1]. This paper presents a parallel analysis from the same experiment of polarization observables with linearly polarized beams for the same reaction. Linearly polarized photons and longitudinally polarized deuterons in a solid hydrogen deuteride (HD) target were used with the CEBAF Large Acceptance Spectrometer (CLAS) at Jefferson lab (JLab). Data are combined to extract the beam (Σ) and beam-target double-polarization (G) asymmetries. Preliminary results for the Σ observables are consistent with existing partial wave analyses (PWA) that incorporate other experiments. Preliminary results for the energy and angular dependence of G are reported; these deviate strongly from existing PWA.

Keywords Meson Photoproduction · Polarization · polarized target · Baryon resonances

PACS 25.20.Lj · 13.88.+e · 14.20.Gk

1 Introduction

Quantum Chromodynamics (QCD) is widely accepted as a successful theory of the strong interaction. However, the spectrum of the nucleon's excited states

H. Y. Lu
University of Iowa
E-mail: hlu@jlab.org

(N* resonances) poses many challenges. In particular both Quark Models and LQCD predict more states than those up to now seen, and this is the so called "missing resonance problem" that it is well discussed in [2–4]. Moreover also quark-diquark models show missing states ([5–10]).In addition, the spectral properties are altered by "dressings", such as meson loops and channel couplings [11]. Although πN scattering data have been intensively analyzed to extract information on N*s, a complete decomposition of the reaction amplitude into multipoles of definite isospin, spin, and parity has not been achieved. Furthermore, while information from both proton and neutron target reactions is required to separate γpN^* and γnN^* couplings and deduce the isospin $I = 1/2$ amplitudes, very little neutron target data is available. Single pseudo-scalar meson photoproduction, such as π production, requires data on a minimum of 8 out of 16 possible spin observables to avoid mathematical ambiguities, and even more when realistic experimental uncertainties are considered [12]. The goal of this work is to provide 2 of them in N* resonance region.

The E06-101 experiment (the *g14* run) at Jefferson Lab with the CEBAF Large Acceptance Spectrometer (CLAS) in Hall B [13], utilized a polarized beam on a polarized target of solid HD [14–16]. During the experiment, both circularly-polarized and linearly-polarized photons were generated by the bremsstrahlung of either polarized electrons or by use of a diamond radiator, respectively. The first beam-target helicity asymmetries with circular beam polarization in the $\gamma n(p) \to \pi^- p(p)$ reaction were reported recently in Ref. [1]. In this work, only reactions produced by linearly-polarized photons were considered, and the beam (Σ) and beam-target (G) helicity asymmetries were extracted over the same energy reagon.

2 Separating asymmetries with double-polarization data

The general expression for the single pseudoscalar-meson production cross section involving a linearly polarized beam and a longitudinally polarized target (summed over final recoil polarization states) is [12]:

$$\frac{d\sigma(P_\gamma, P_D)}{d\Omega} = \frac{d\sigma_0}{d\Omega}\left(1 - P_\gamma^L \Sigma(\theta; W) cos(2\phi) + P_\gamma^L P_D^V G(\theta; W) sin(2\phi)\right), \quad (1)$$

where σ_0 is a constant independent of beam or target polarization, P_γ^L is the degree of beam linear polarization, P_D^V is the vector polarization of the deuteron along the beam axis Z, and ϕ is the azimuthal angle relative to the beam polarization plane; Σ and G are beam and beam-target asymmetries, respectively. The linear beam polarization plane is either X-Z plane or Y-Z plane. Suppose for an arbitrary detector element, the azimuthal angle is ϕ relative to X-Z plane. Then its azimuthal angle relative to Y-Z plane is $\frac{\pi}{2} + \phi$. The $cos(2\phi)$ term in Eqn. 1 will give opposite signs for these cases. The target polarization is either +Z or -Z. The P_D^V term will give two opposite signs. All combinations of beam and target polarization give four configurations: (1) beam polarization direction along $\phi = 0$ degrees and target polarization along

+Z direction; (2) beam along $\phi = 0$ degrees and target along -Z; (3) beam along $\phi = 90$ degrees and target along +Z; (4) beam along $\phi = 90$ degrees and target at -Z. The yields of these four configurations at a given angle are:

$$\begin{aligned} Y_1 &= L_1 A \Delta\Omega \frac{d\sigma_0}{d\Omega} \left(1 - p_1 \Sigma cos(2\phi) + p_1 p_+ G sin(2\phi)\right) \\ Y_2 &= L_2 A \Delta\Omega \frac{d\sigma_0}{d\Omega} \left(1 - p_2 \Sigma cos(2\phi) - p_2 p_- G sin(2\phi)\right) \\ Y_3 &= L_3 A \Delta\Omega \frac{d\sigma_0}{d\Omega} \left(1 + p_3 \Sigma cos(2\phi) + p_3 p_+ G sin(2\phi)\right) \\ Y_4 &= L_4 A \Delta\Omega \frac{d\sigma_0}{d\Omega} \left(1 + p_4 \Sigma cos(2\phi) - p_4 p_- G sin(2\phi)\right), \end{aligned} \tag{2}$$

where L_i is the luminosity for each configuration, A is the acceptance which is approximately the same for all the configurations when $\Delta\Omega$ the solid angle of each bin is large enough, p_i is the average photon beam polarization of each configuration, p_+ and p_- are the magnitudes of the target polarization along the +Z and -Z direction. By using simple algebra, terms in Σ and in G can be evaluated independently as:

$$\begin{aligned} \Sigma cos(2\phi) &= \frac{s_1 Y_1 + s_2 Y_2 + s_3 Y_3 + s_4 Y_4}{a_1 Y_1 + a_2 Y_2 + a_3 Y_3 + a_4 Y_4} \\ G sin(2\phi) &= \frac{g_1 Y_1 + g_2 Y_2 + g_3 Y_3 + g_4 Y_4}{a_1 Y_1 + a_2 Y_2 + a_3 Y_3 + a_4 Y_4}, \end{aligned} \tag{3}$$

where the coefficients for Σ are:

$$\begin{aligned} s_1 &= \frac{-(p_-) p_2 C_0}{N_1} \\ s_2 &= \frac{-(p_+) p_1 C_0}{N_2} \\ s_3 &= \frac{(p_-) p_4 C_{90}}{N_3} \\ s_4 &= \frac{(p_+) p_3 C_{90}}{N_4} \\ a_1 &= \frac{(p_-) D}{N_1 p_1} \\ a_2 &= \frac{(p_+) D}{N_2 p_2} \\ a_3 &= \frac{(p_-) D}{N_3 p_3} \\ a_4 &= \frac{(p_+) D}{N_4 p_4}. \end{aligned} \tag{4}$$

Here, N_i is the product of a constant with L_i and

$$\begin{aligned} C_0 &= p_4 p_- + p_3 p_+ \\ C_{90} &= p_2 p_- + p_1 p_+ \\ D &= p_1 p_2 p_3 p_4. \end{aligned} \tag{5}$$

The normalization factors N_i are extracted from the reconstructed reaction yields originating in a foil that is independent of the target (see Sect. 3.4). It is convenient to express the coefficients for G in terms of a new variable, defined as:

$$E = (p_1 + p_3) p_2 p_4 p_- + (p_2 + p_4) p_1 p_3 p_+. \tag{6}$$

Then the coefficients for G are:

$$\begin{aligned} g_1 &= \frac{E p_2}{N_1} \\ g_2 &= \frac{E p_1}{N_2} \\ g_3 &= \frac{E p_4}{N_3} \\ g_4 &= \frac{E p_3}{N_4}. \end{aligned} \tag{7}$$

With these coefficients evaluated for the four different sets of run conditions, Σ and G can be extracted, independent of one another, from Eqn. 3 by fitting $cos(2\phi)$ and $sin(2\phi)$ distributions. This use of all four initial state polarization configurations has a significant practical advantage in controlling the systematic uncertainties. While a fit of the ϕ dependence in any one of the yields of Eqn. 2 could in principle separate the Σ and G terms, in practice when G is small its contribution appears only as a slight phase shift to the Σ asymmetry.

3 Event Selection, Cuts and Corrections

To minimize the statistical and systematical uncertainties simultaneously, a series of data selection cuts have been applied and checked. There are four major cuts and one correction that has been applied in this work. These are described in the following sections.

3.1 Timing Requirements

In each event, timing and energy information of many photons are recorded. However, only one photon generates the event. In order to find the correct photon and discard the events where no correct photon information can be found, a timing cut is applied.

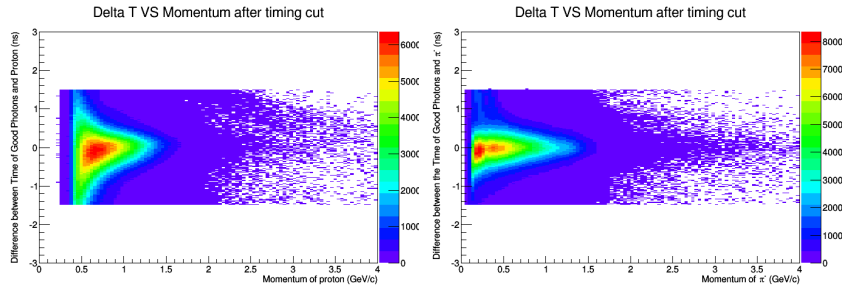

Fig. 1 Time difference between Proton (left) or π^- (right) and photon verses their momenta, respectively. (See Sect. 3.1.)

First, events with two (and only two) reconstructed charged particles are selected. The particle with a positive charge is assumed to be a proton, and the one with a negative charge is assumed to be a π^-. The production times of these two particles at the target center are calculated from their track length, the hit time at the time-of-flight counters, and from the momentum for each particle as measured in CLAS. These are compared with the photon arrival time at the target center in Figure 1, which shows the difference between the particle creation times and photon arrival times for protons (left panel) and π^- (right panel). A requirement of 0 ± 1.5 ns is placed on each of these time differences. Every event within this selection is consistent with the assumption that a photon reacts in the target and generates a proton and a π^- with consistent timing.

3.2 Exclusivity Requirements

In Sect. 3.1, only the timing information is considered. The missing mass after the above requirements is shown in blue on the left side of Fig. 3. The peak at $0.9 GeV/c^2$ is mainly from a spectator proton. The events other than the peak are from either inclusive production of $p\pi^-$ or other production channel whose timing is accidentally coincident. In order to select the events from the exclusive $p\pi^-$ production, an exclusive cut is performed using the following sequence of steps.

1. Calculate the momentum of the initial-state neutron in Deuterium from the detected proton and π^-, assuming a two-body reaction and momentum conservation. With this, calculate the boost needed to reach the center-of-mass frame of the photon and the target neutron with its non-zero momentum.
2. Calculate the expected momentum of the proton in this center-of-mass frame, p_1, by assuming the two-body reaction $\gamma n \to p\pi^-$.
3. Boost the detected proton momentum (p_2) into this same center-of-mass frame and calculate the difference $\Delta p = p_1 - p_2$. This Δp is plotted against missing mass at the left in Fig. 2. The exclusive production events are

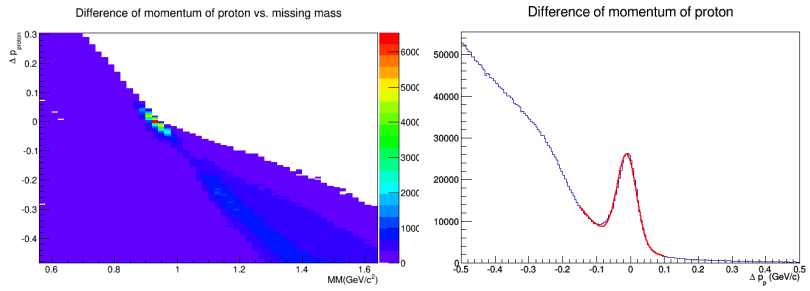

Fig. 2 Left: difference between the measured and theoretical momenta of protons plotted against missing mass; right: projection of the left panel onto the vertical axis, and a fit of the momentum difference to a Gaussian peak with a polynomial background . (See Sect. 3.2.)

concentrated in the area with y-coordinate around 0 and x-coordinate just below 1 GeV/c^2.

4. The distribution of Δp is shown in the right panel of Fig. 2. A fit to a Gaussian distribution with a polynomial background is used to obtain the red curve. A 3-σ cut around the peak is applied to select the events of interest.

This *exclusivity* cut is very efficient. Figure 3 shows the missing mass of rejected events (those outside of the above 3σ selection) as the red histogram in the left panel, and the azimuthal angle between the proton and the π^- for accepted events in the right panel. In the missing mass plot, it is clear that the rejected distribution (red) is consistent with the background of all events (blue) before the cut. This process leaves a set of very pure exclusive production events for the next steps of analysis. The azimuthal-angle difference distribution for events passing these *exclusivity* requirements confirms this purity by displaying two isolated peaks at ± 180 degrees in the right panel, as expected for a two-body reaction.

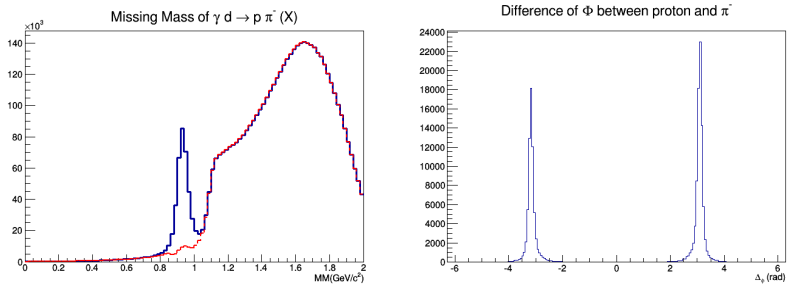

Fig. 3 Left: missing mass before selection (blue) and cut away(red); right: ϕ angle between proton and π^-.

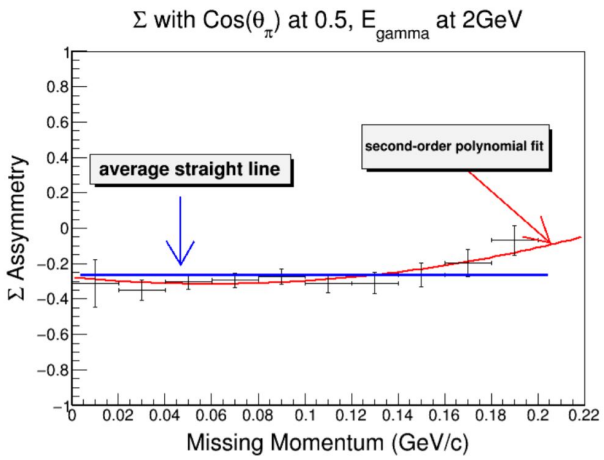

Fig. 4 Σ with different missing-momentum selections.

3.3 Missing Momentum Selection

As the momentum of the undetected proton in the $p\pi^-(p)$ final state increases, the potential grows for contributions from complex final state interactions (FSI), which are not associated with the quasi-free $\gamma + n$ process of interest. While this favors a tight cut on the missing momentum, it comes at the cost of statistical uncertainty. Rather than invoking theoretical arguments, we have let the data itself determine the optimal maximum momentum. The missing-momentum dependence of Σ is shown in Fig. 4. Σ values are essentially independent of missing momentum below 0.18 GeV/c, beyond which they begin to rise. A second-order polynomial function (red curve) extrapolates the value to zero-missing momentum, which is very close to the average value. A maximal missing momentum of 0.2 GeV/c has been adopted for the results discussed here.

3.4 Dilution Factor and Reaction Vertex Requirement

Figure 5 shows the vertex distribution from an empty target cell. There are three dominant peaks from Kel-F (C_2ClF_3). The first two (at Z = -11 and -5 cm) arise from the beam entrance and exit windows of the target cell. Between these there exist auxiliary aluminum cooling wires (and target material when a cell full of HD is used). The third major peak (at Z = +1 cm) is part of the cryostat and independent of the target. The latter provides a source that can be used to flux-normalize HD production runs with different polarization configurations, and compare with empty target runs. In this analysis, the target material area is defined as the region from Z = -9.6 to -6.9 cm (between red lines in Fig. 5). Events inside this target material area are finally chosen to extract asymmetries.

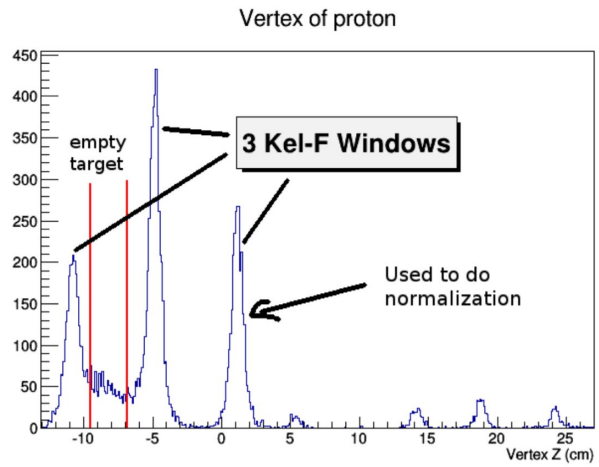

Fig. 5 Vertex distribution from an empty target.

The aluminum within the target material area of Fig. 5 is not polarized and cannot contribute to the asymmetries. It dilutes the asymmetry values and needs to be corrected. We construct a dilution factor as:

$$f_{dilution} = \frac{N_p}{N_p - N_e} \tag{8}$$

where N_p and N_e are number of flux-normalized events in the target material area from production-target and empty-target runs, respectively. This dilution factor is a correction which multiplies with the extracted asymmetry values. The production (full target) vertex distribution is shown together with empty-target data in the left panel of Fig. 6 as the red and blue histograms, respectively. They are normalized by matching the number of events in the normalization area around the $Z = +1$ Kel-F peak. The normalization area is determined by the region of integration around this $Z = +1$ cm peak, as

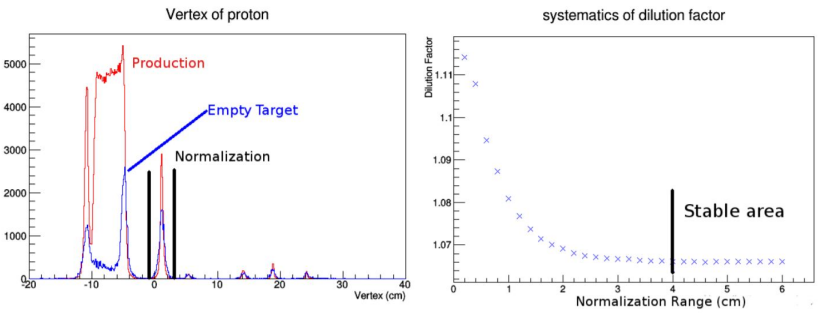

Fig. 6 Left: Production vertex distribution in red and empty target in blue; right: dilution factor dependence on the width of the normalization area.

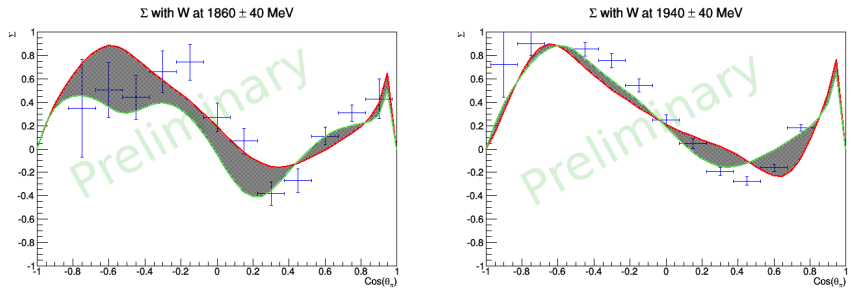

Fig. 7 Σ dependence on $cos(\theta_\pi)$ with SAID model predictions. Points with error bars are from this work for the W ranges from 1820 to 1900 MeV (left), and from 1900 to 1980 MeV (right). The shaded region shows the SAID predictions bounded by the upper and lower limits of the invariant mass interval.

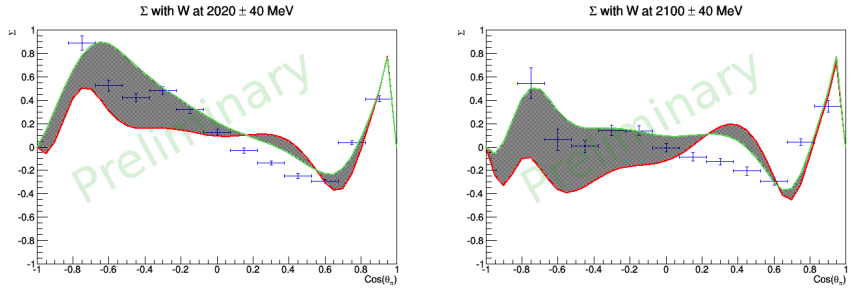

Fig. 8 Σ dependence on $cos(\theta_\pi)$ with SAID model predictions. Points with error bars are from this work for the W ranges from 1980 to 2060 MeV (left), and from 2060 to 2140 MeV (right). Shaded regions are as in Fig. 7.

indicated by the two vertical lines. When this interval is varied, the dilution factor varies as shown on the right side of Fig. 6. When the width of the interval is greater than 4 cm, the value is stable. The final value is taken as the average of the stable values, namely 1.066.

4 results

Using events that pass through all the selection criteria, Σ and G are separated with the method described in Sect. 2. The results for Σ are shown in Figs. 7 and 8, while the results for G are plotted in Figs. 9 and 10.

The predictions of SAID partial wave analysis (PWA) are also shown in these figures. (These SAID PWA have not yet been fitted to these new asymmetry data.) The shaded areas are the PWA prediction for the corresponding W range. As shown, the Σ results are in quite good agreement with the model prediction, while the G results are generally very much smaller than the PWA values. Because of these large differences, we expect these new G results to have a significant impact on future PWA, and through them on the determination of N* resonance parameters.

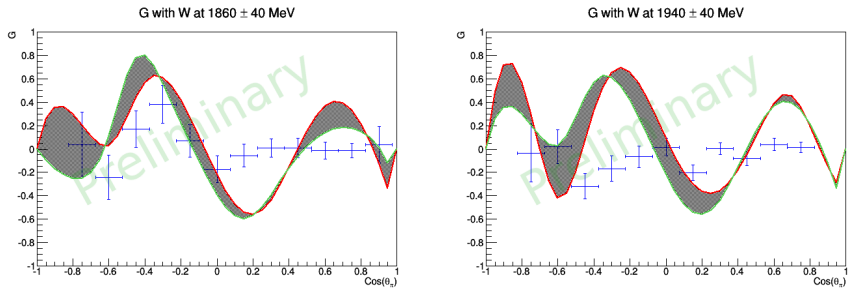

Fig. 9 G dependence on $cos(\theta_\pi)$ with SAID model predictions. Points with error bars are from this work for the W ranges from 1820 to 1900 MeV (left), and from 1900 to 1980 MeV (right). Shaded regions are as in Fig. 7.

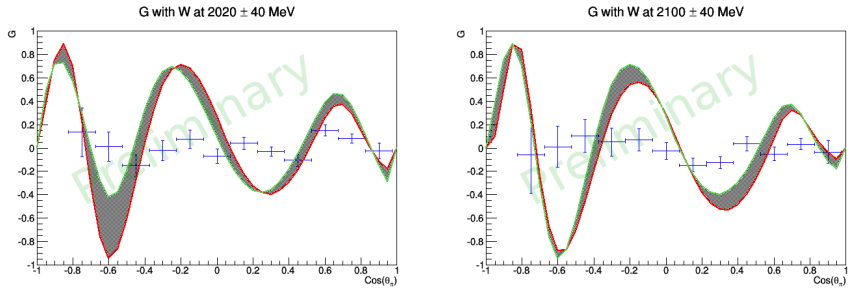

Fig. 10 G dependence on $cos(\theta_\pi)$ with SAID model predictions. Points with error bars are from this work for the W ranges from 1980 to 2060 MeV (left), and from 2060 to 2140 MeV (right). Shaded regions are as in Fig. 7.

Acknowledgements This work was supported by the U.S. Department of Energy, Office of Nuclear Physics Division, under Contract No. DE-AC05-06OR23177, under which Jefferson Science Associates operate Jefferson Laboratory, by the US National Science Foundation, and by the funding agencies of CLAS collaboration members.

References

1. D. Hao *et al.*, Beam-Target Helicity Asymmetry for $\boldsymbol{\gamma n} \to \pi^- p$ in the N* Resonance Region, PRL, 118, 242002 (2017)
2. R. Bijker *et al.*, Strong Decays of Baryons and Missing Resonances, PRD, 94, 074040 (2016)
3. N. Isgur and G. Karl, *P*-Wave Baryons in the Quark Model, PRD, 18, 4187 (1978); ibid. D19, 2653 (1979); ibid. D20, 1191 (1979)
4. M. Giannini *et al.*, The Hypercentral Constituent Quark Model and its Application to Baryon Properties, Chin. J. Phys. 53, 020301 (2015)
5. R.L. Jaffe, Exotica, Phys. Rept. 409, 1 (2005)
6. E. Santopinto, Interacting Quark-Diquark Model of Baryons, Phys. Rev. C 72, 022201 (2005)
7. J. Ferretti *et al.*, Relativisitc Quark-Diquark model of Baryons, Phys. Rev. C 83, 065204 (2011)
8. M.De Sanctis et al. , Electromagnetic Form Factors in the Relativistic Interacting Quark-Diquark Model of Baryons, Phys. Rev. C 84 (2011) 055201; Eur. Phys. J. A 52, 121 (2016)

9. E. Santopinto and J. Ferretti, Strange and Nonstrange Baryon Spectra in the Relativistic Interacting Quark-Diquark Model with a Gürsey and Radicati-inspired Exchange Interaction, Phys. Rev. C 92, 025202 (2015)
10. G. Galata and E. Santopinto, Hybrid Quark-Diquark Baryon Model, Phys. Rev. C 86, 045202 (2012)
11. N. Suzuki *et al.*, Disentangling the Dynamical Origin of P_{11} Nucleon Resonances, PRL, 104, 042302 (2010)
12. A. M. Sandorfi *et al.*, Determining pseudoscalar meson photoproduction amplitudes from complete experiments, J. of Phys. G, 38, 053001 (2011)
13. B. A. Mecking *et al.*, The CEBAF Large Acceptance Spectrometer (CLAS), Nucl. Instrum. Meth. A, 503, 513 (2003)
14. C. D. Bass *et al.*, A Portable Cryostat for the Cold Transfer of Polarized Solid HD Targets: HD-Ice-I, Nucl. Instrum. Meth. A, 737, 107 (2014)
15. M. M. Lowry *et al.*, A Cryostat to Hold Frozen-Spin Polarized HD Targets in CLAS: HDice-II, Nucl. Instrum. Meth. A, 815, 31 (2016)
16. X. Wei *et al.*, Boosting Deuteron Polarization in HD Targets: Experience of moving spins between H and D with RF methods during the E06-101 experiment at Jefferson Lab, PoS, PSTP2013, 016 (2014)